Sol–gel synthesis, optical and structural characterization of ZrOS nanopowder

U. C. Uduh, R. M. Obodo, S. Esaenwi, C. I. Amaechi, P. U. Asogwa, R. U. Osuji & F. I. Ezema

Journal of Sol-Gel Science and Technology

ISSN 0928-0707

J Sol-Gel Sci Technol
DOI 10.1007/s10971-014-3331-7

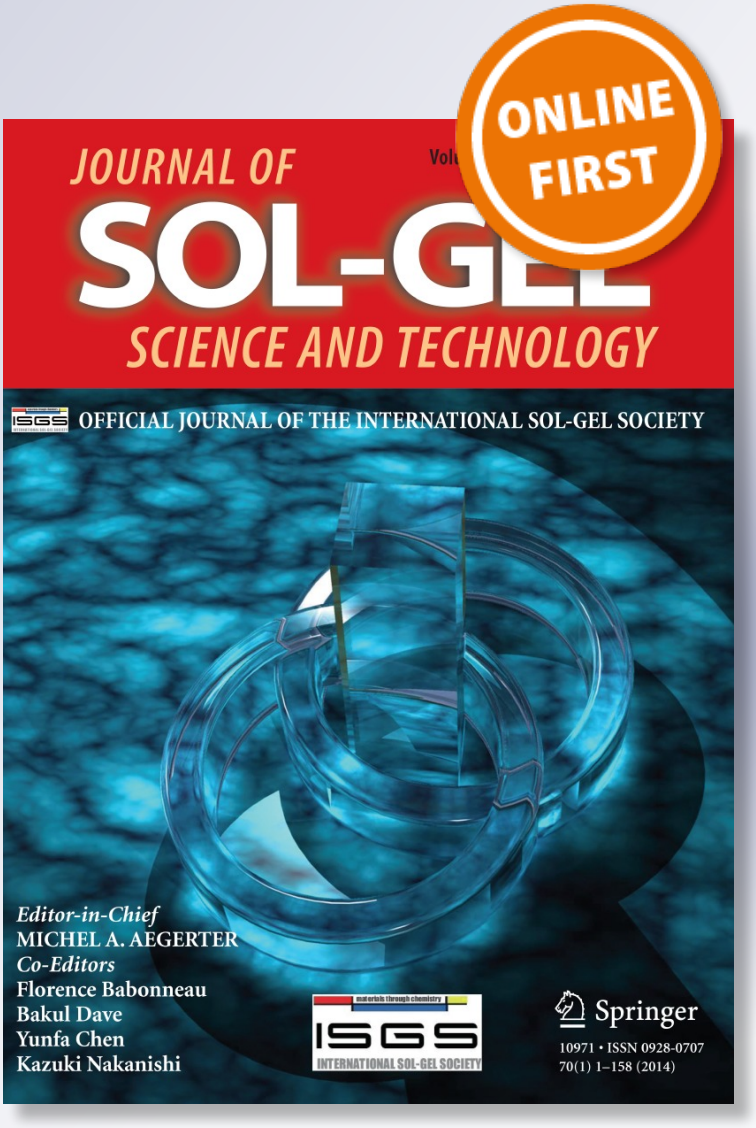

Springer

J Sol-Gel Sci Technol
DOI 10.1007/s10971-014-3331-7

ORIGINAL PAPER

Sol–gel synthesis, optical and structural characterization of ZrOS nanopowder

U. C. Uduh · R. M. Obodo · S. Esaenwi · C. I. Amaechi · P. U. Asogwa · R. U. Osuji · F. I. Ezema

Received: 10 December 2013 / Accepted: 15 March 2014

Abstract In this paper, we report the synthesis of tetragonal zirconium oxysulfide *t*-ZrOS nanopowder by the sol–gel method using water solution of a precursor containing thiourea $[CS(NH_2)_2]$ and zirconium in the form of an anionic oxalate complex $[Zr(C_2O_4)]^{4-}$. The tetragonal *t*-ZrOS structure with space group P4/nmm revealed by X-ray patterns showed preferred orientation along (101) plane. For surface morphology, compositional and optical absorption studies, scanning electron microscopy, energy dispersive X-ray and ultraviolet–visible spectroscopy were employed for characterization of the powder respectively. A nearly constant value of the refractive index at higher wavelength $\lambda \geq 1{,}100$ nm was found to be 2.19. High indirect and direct optical band gap of $\sim$2.0 and 2.50 eV with absorbance <40 % were obtained for the powder.

Keywords Tetragonal ZrOS nanopowder · Anionic oxalate complex · Sol–gel technique · Absorbance

1 Introduction

The exhibition of both metallic and covalent bonding characteristics by fourth column transition metals have been considered as semiconductors with layered structure. Three polymorphic forms of zirconia exist at atmospheric pressure depending on temperature. They are monoclinic, *m*-ZrO_2 (baddeleyite, $a = 5.121$ Å, $b = 5.19$ Å, $c = 5.316$ Å, $\beta = 98.83^{\circ}$), tetragonal, *t*-ZrO_2 with lattice parameters $a = 3.632$ Å, $c = 5.075$ Å and cubic, *c*-ZrO_2 ($a = 5.128$ Å). Their transition temperatures are not accurately known but it is assumed that the monoclinic form is stable up to $\sim$1,100 °C, while above 2,300 °C the stable form is cubic structure [1]. However, appearance of both cubic and tetragonal metastable phases at low temperature (LT) has been observed by numerous authors and this situation is ascribed to precursor materials, preparative condition, presence of impurities and dopants.

Even though, preparation of pseudo-tetragonal $ZrO_{0.75}S$ and its electric responses on temperature and frequency related to microstructural relaxation has been reported [2], recently a considerable amount of work has been reported on the properties of rare earth-doped ZrO_2, such as ZrO_2:Eu [3, 4], ZrO_2:Er [5, 6] and ZrO_2:Sm [7–9]. The lanthanide ions incorporation into zirconia materials can achieve special optical properties due to structural modifications, thereby impacting the electronic structure of the lattice host material [10]. Notwithstanding the conjugate form (pure or mixed with other oxides), zirconium based materials have formed basis for high-performance structural engineering ceramics, ceramic electrolytes used in oxygen monitors [11] and fuel cells [12] which have been developed. It is widely applied as catalyst especially in cases when durability to chemical attack is required [13]. Thick and thin films of zirconia are used as thermal oxidation and corrosion barrier coatings for protection of stainless steel [14], overcoats for thin film media of magnetic recording discs and buffer layers in processing of high-temperature superconducting thin film devices [15].

U. C. Uduh · R. M. Obodo · S. Esaenwi · C. I. Amaechi (✉) · P. U. Asogwa · R. U. Osuji · F. I. Ezema
Department of Physics and Astronomy, University of Nigeria, Nsukka, Enugu State, Nigeria
e-mail: ifeanyichukwuonline@yahoo.com

S. Esaenwi
Centre for Basic Space Sciences, National Space Research and Development Agency, University of Nigeria, Nsukka, Enugu State, Nigeria

Published online: 26 March 2014

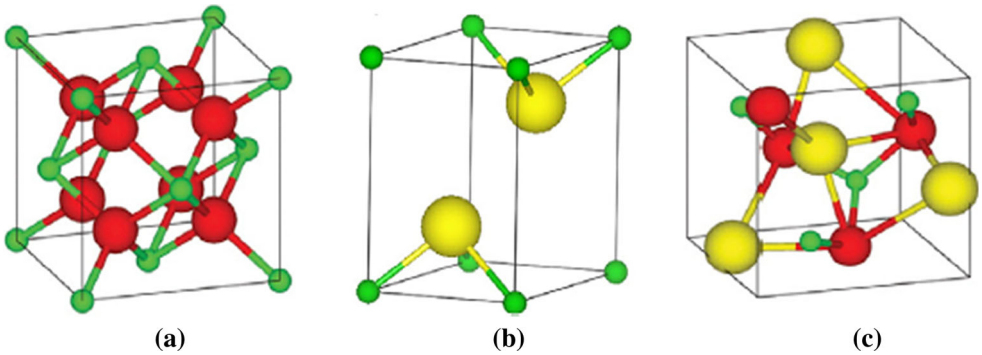

Fig. 1 Structures of **a** *c*—ZrO_2 **b** ZrS_2 and **c** ZrOS. The *red spheres* are oxygen ions, *green spheres* are zirconium ions, and *yellow spheres* are sulfur ions (Color figure online)

Now, considering metal oxide, metal sulfide and metal oxysulfide such as the ZrO_2, ZrS_2 and ZrOS, they have different structures (Fig. 1a–c) and different properties even though the oxygen and sulfur belong to same group in periodic table. We know well the sulfur is larger in size, less electronegative, and the *d*-orbital of sulfur is available for bonding. ZrOS with cubic structure has been first prepared by passage of H_2S over $Zr(SO_4)_2$ at red heat [16], by passing H_2S through a graphite tube containing ZrO_2 at 1,300 °C [17], and formation and migration of oxygen and zirconium vacancies in cubic zirconia and zirconium oxysulfide [18] but no exhaustive optical properties of the material have been studied yet, although optical properties of ZrO_2 and ZrS_2 have been well known. Particles of ZrOS have been synthesized by different chemical techniques/routes but the advantages offered by sol–gel method have shown superiority to the conventional solid state reaction because of possibility of mixing starting materials at the molecular level and resulting product expected to be homogenous [19].

Therefore, in this paper, we report the preparation of zirconium based powder from a solution of thiourea and zirconium oxychloride octahydrate ($ZrOCl_2{\cdot}8H_2O$) in the form of an anionic oxalate complex using a low cost and simple wet-chemical method, sol–gel. Morphological evolution, optical absorption studies and structural properties of the calcinated ZrOS powder is equally presented.

2 Experimental details

2.1 Material synthesis

Analytical reagent grade zirconium oxychloride, $ZrOCl_2{\cdot}8H_2O$ (Aldrich, 98 %) and oxalic acid, $(COOH)_2{\cdot}2H_2O$ (Aldrich, 99 %) were used for the preparation of the precursor as an anoionic oxalate complex, while thiourea, $(CS(NH_2)_2)$ (Aldrich, 99 %) was the sulphiding agent. ZrOS powder was synthesized by adding soluble inorganic salt, 1 M 30 mL $ZrOCl_2{\cdot}8H_2O$, 1 M 30 mL $CS(NH_2)_2$ and stoichiometric quantity of 1 M 30 mL oxalic acid at ambient temperature. Then the overall solution was heated by means of magnetic heater/stirrer for 30 min at 80 °C. Silicate substrates were degreased in acetone solution and ultrasonically cleansed in deionized water for 20 s. Optical absorption studies were carried out by dip-coating of silicate substrates in the gel for 5 min. After rinsing in deionized water, they were drip-dried in air. Later the bath content was evaporated to dryness at 100 °C for 2 h. Then, a white xerogel is formed. This xerogel is the precursor of the hydrated ZrOS powder. ZrOS powders were then obtained after calcination of the xerogel in air atmospheric pressure and at a bit high temperature (450 °C, 2 h). The milled powder obtained after calcination appeared whitish-ash in color showing complete decomposition of the oxalate ligands.

2.2 Characterization of ZrOS powder

Crystallinity of the obtained powder was studied using X-ray diffraction (XRD). The patterns were obtained on a PANalytical diffractometer equipped with a graphite monochromator using CuKα radiation ($\lambda = 1.5406$ Å). These patterns were scanning in steps of 0.05° within the 2θ range 20°–80° with the constant counting time. Scanning electron microscopy (SEM) with the SEM 515 Philips instrument was applied in surface morphology observation of the particles, while its elemental composition was investigated by energy dispersive X-ray (EDX) spectroscopy. Absorption spectra studies were recorded using UNICO-UV–Vis-NIR 2102 PC spectrophotometer in the range of 300–1,100 nm with sample in the radiation path.

3 Results and discussion

3.1 X-ray diffraction analyses

Figure 2 shows an overview of XRD patterns for sol–gel grown ZrOS powder, which was exposed to 2 h isothermal

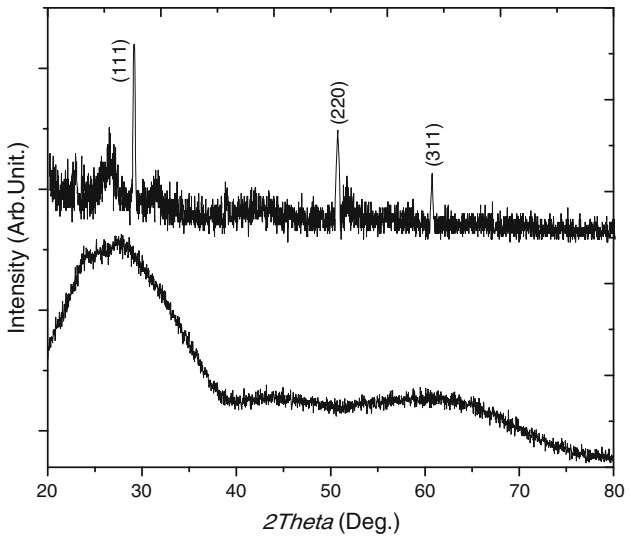

Fig. 2 XRD pattern of tetragonal ZrOS powder calcinated isothermally at 450 °C for 2 h

calcinations at 450 °C. As it can be seen, the pattern possesses peaks which would be evident if calcination temperature were increased beyond 450 °C. However, thermal treatment of the xerogel reveals an amorphous to polycrystalline material accompanied by a tetragonal zirconia, *t*-ZrOS which is stable in this temperature region. This is supported by the literature [20–23] asserting that the formation of metastable tetragonal zirconia occurs in all cases during LT calcination of powdery material films and coatings. However, there is a significant composition of the amorphous domain in the calcinated powdery zirconia.

The tetragonal *t*-ZrOS in space group of P4/nmm with cell dimensions of $a = 3.55$ Å and $c = 6.31$ Å against the cubic *c*-ZrOS in space group $P2_13$ with cell dimension of $a = 5.696$ Å is known as the alternative phase of ZrOS, and it is an iso-structure of PbFCl-type which is a layered structure with Cl–Cl Van der Waals interactions between layers [24]. The XRD pattern of the isothermal calcinated ZrOS powder revealed peak values around 30.50°, 50.60° and 60.99° with preferred orientations at (111), (220) and (311) respectively [ICSD 01-085-1081]. The indexing at the aforesaid orientations is in strong agreement with the report of Mikó et al. [25]. XRD line broadening was used to estimate the particle size of the powder by employing inverse proportional relation of full width at half maximum (FWHM) as predicted by Debye–Scherrer's equation [26]:

$$D = \frac{k\lambda}{\beta_{2\phi} Cos\phi} \tag{1}$$

where $k = 0.89$ is a correction factor, λ is the wavelength of X-ray (CuKα radiation $\lambda = 1.5406$ Å), ϕ the Bragg's angle of reflection, $\beta_{2\phi}$ is the FWHM of most intense diffraction plane.

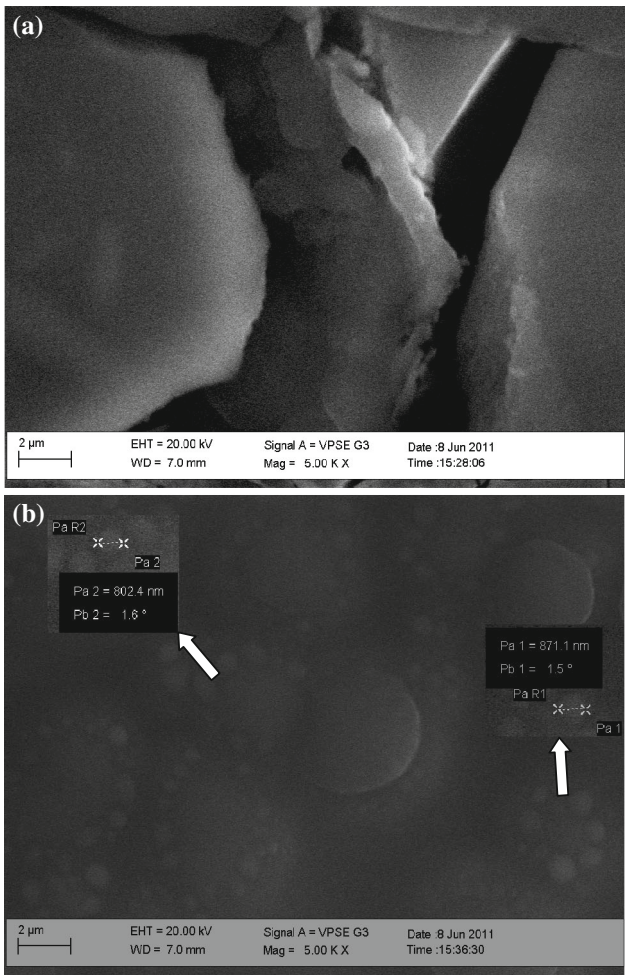

Fig. 3 Scanning electron microscopy of **a** as-deposited isothermally calcinated tetragonal ZrOS powder, **b** isothermally calcinated milled tetragonal ZrOS powder

The average particle size of *t*-ZrOS powder deduced was found to be ~13.6–15.2 nm which is in agreement with the report of Mikó et al. [25] and Joy et al. [27]. The interplanar spacing as proposed by Bragg's law is equated with the interatomic spacing for the tetragonal phase crystalline structure yielding an interatomic distance of 0.152 nm as given by the equation:

$$d_{hkl} = \frac{n\lambda}{2\sin\phi} = \left[\frac{h^2 + k^2}{a^2} + \frac{l^2}{c^2}\right]^{-\frac{1}{2}} \tag{2}$$

3.2 Morphological characterization

The SEM (5000×) of isothermally treated sulfur mediated zirconium oxide *t*-ZrOS powder is displayed in Fig. 3a. It shows that the dense surface appears slightly granular having different sizes and shapes of grains with many

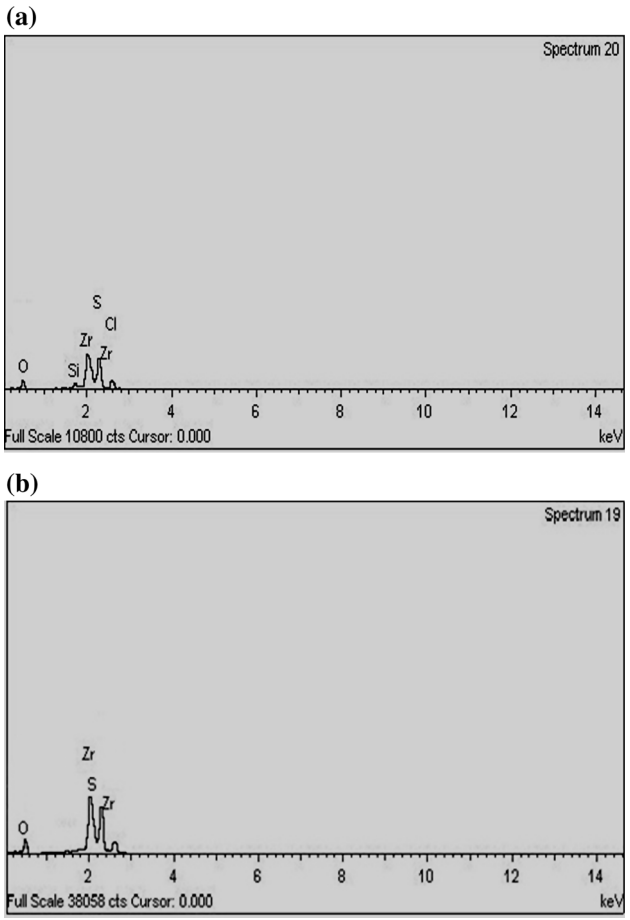

Fig. 4 EDX spectroscopy of **a** ZrOS coated on silicate substrate, **b** isothermally calcinated ZrOS powder showing complete removal of chlorine

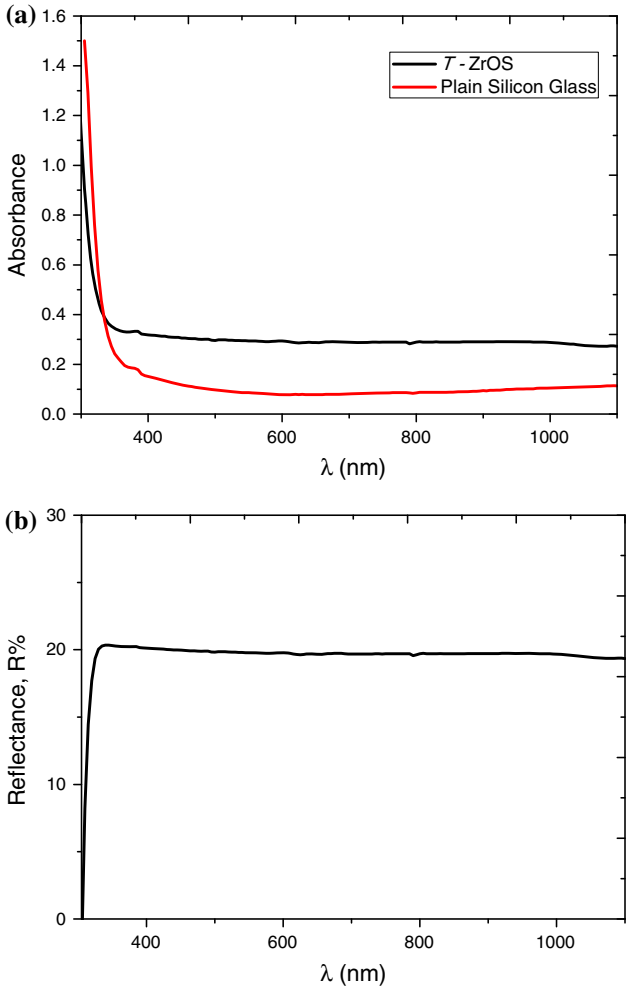

Fig. 5 **a** Absorbance spectrum of sol–gel dip coated tetragonal ZrOS on silicate substrate, **b** reflectance spectrum of sol–gel dip coated tetragonal ZrOS on silicate substrate

cracks generated on the surface. This effect exhibited by photomicrographs may be due to rise in calcination temperature accompanied by crystallization and this culminates in roughening of the surface with proliferated cracks. The as-deposited particulates (before milling) (Fig. 3b) has a non-uniform rough surface without structural order, which suggests amorphous nature of the powder. The average measured diameter of randomly distributed grains was distributed in the range of 800–900 nm.

3.3 Energy dispersive X-ray analysis

Energy dispersive X-ray of tetragonal ZrOS as well as isothermal calcinated *t*-ZrOS powder is examined. An EDX patterns Fig. 4a, b shows the presence of sulfur in zirconium oxide of sol–gel dip-coated silicon substrate and calcinated powder. The complete removal of chlorine in EDX of powdery ZrOS is also confirmed in Fig. 5b. The EDX spectrum shows the presence of two peaks associated with the O (11.49 %) and Zr (65.49 %) by weight. The sulfur, S^{2-} ions percentage in the matrix is about 23.02 %. In general, the molecular computation agrees with stoichiometry of ZrOS.

3.4 Optical absorption studies

The optical properties and the possible electronic transitions of tetragonal ZrOS powder were determined from the recorded transmission and reflection spectra. The ambient temperature optical absorbance and reflectance spectra of tetragonal sulfur mediated zirconia powder recorded in wavelength range 300–1,100 nm are shown in Fig. 5a, b. From the absorption spectrum, it is clear that sol–gel dip-coated *t*-ZrOS on silicate substrate has slightly less-than-average absorbance of light in the visible region, indicating applicability as fairly absorbing material. This development (low absorbance), suggests that the dip-coated film of ZrOS is not fully oxidized or affected by silicon substrate.

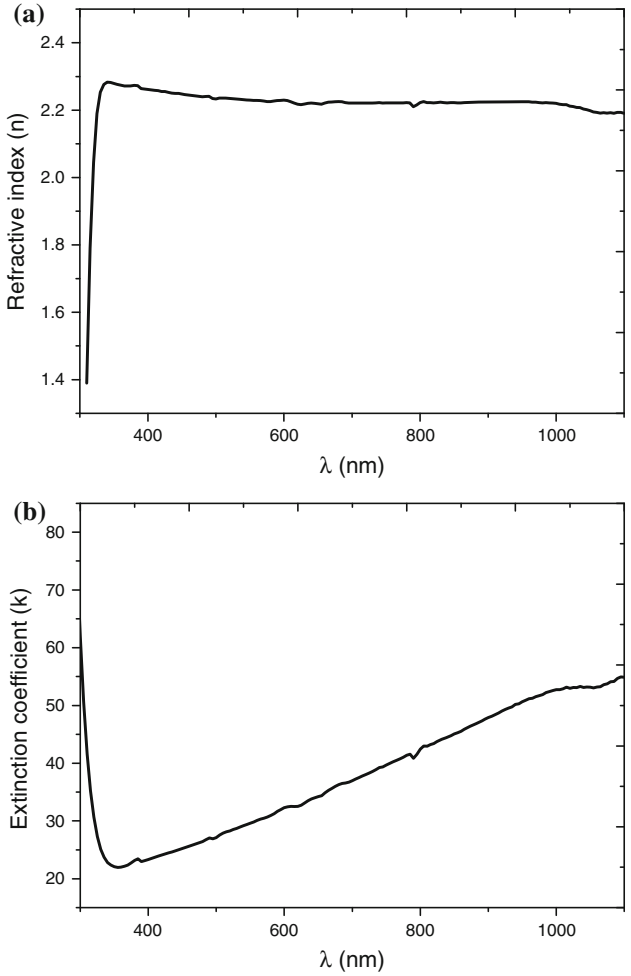

Fig. 6 The spectral variation of **a** refractive index with wavelength of sol–gel dip coated tetragonal ZrOS on silicate substrate, **b** extinction coefficient with wavelength of sol–gel dip coated tetragonal ZrOS on silicate substrate

Again, the cracks observed by SEM support the fact that the films was not of optical quality. The reflectivity of a material of refractive index n, and extinction coefficient, k is given by [28]:

$$R = \frac{n^2 - 1 + k^2}{n^2 + 1 + k^2} \tag{3}$$

The transmission in the absence of interference fringes of a thin film deposited on perfectly smooth substrate is given by [29, 30]:

$$T = \frac{(1-R)^2 e^{-\alpha t}}{1 - R^2 e^{-2\alpha t}} \tag{4}$$

where $\alpha = \frac{4\pi k}{\lambda}$ is the absorption coefficient. By using these relations, n and k may be determined from the measurement of T and R using suitable computer program.

Figure 6a, b show the spectral variation of the refractive index and extinction coefficient versus wavelength, λ. The

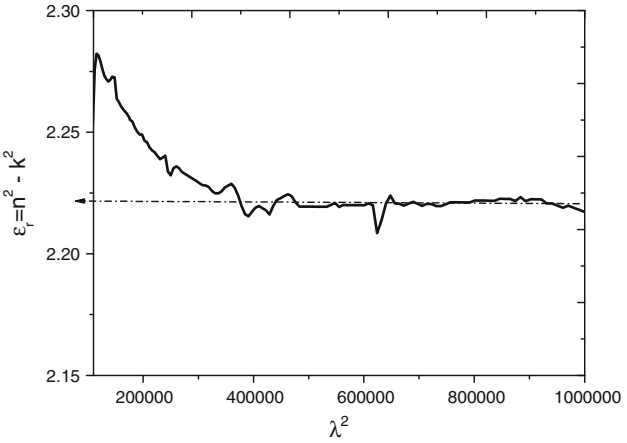

Fig. 7 Plot of real part of dielectric constant ε_r in the wavelength range 300–1100 nm

variation assumes a rapid increase within the UV region. However, there is slight stability of this variation in the visible region and NIR. It is seen that the refractive index has peak in the dispersion region near ~340 nm. Thereafter, n tends to decrease slightly with increasing wavelength. The nearly constant value of refractive index, n_∞, at higher wavelengths ($\lambda \geq 1100$ nm) was found to be 2.19.

According to Spitzer and Fan [31], the real component of the dielectric constant, ε_r is related to the square of wavelength, λ^2 by Eq. 5:

$$\varepsilon_r = n^2 - k^2 = \varepsilon_\infty - \left[\frac{e^2}{\pi c^2}\right]\frac{N}{m^*}\lambda^2 \tag{5}$$

where e is the electronic charge, c the speed of light, N the carrier concentration and m* the effective mass. Plotting $\varepsilon_r = n^2 - k^2$ versus λ^2 as shown in Fig. 7 for t-ZrOS powder, the intercept on ε_r axis (i.e. $\lambda^2 = 0$) for the linear part at higher wavelengths gives the high frequency dielectric constant ε_∞, and the slope gives the carrier concentration to effective mass ratio, N/m*. The estimated values of ε_∞ and N/m* were found to be 2.22 and $9.72 \times 10^{37}\text{cm}^{-3}$.

It is observed that the dielectric constant varies in the range 2.20–2.30, with its minimum in the visible region making it a prospective candidate for dielectric material. Upon comparison, the dielectric constant (2.22) under study shows agreement with the report of Reyna-Garcia et al. [32].

Using the average value of extinction coefficient k, at certain wavelength λ, the absorption coefficient α can be calculated. Inset of Fig. 8a shows the variation of absorption coefficient as a function of photon energy. The absorption coefficient changes from 5.56×10^8 to $3.43 \times 10^9\text{cm}^{-1}$ in the photon energy range 1.0–4.25 eV.

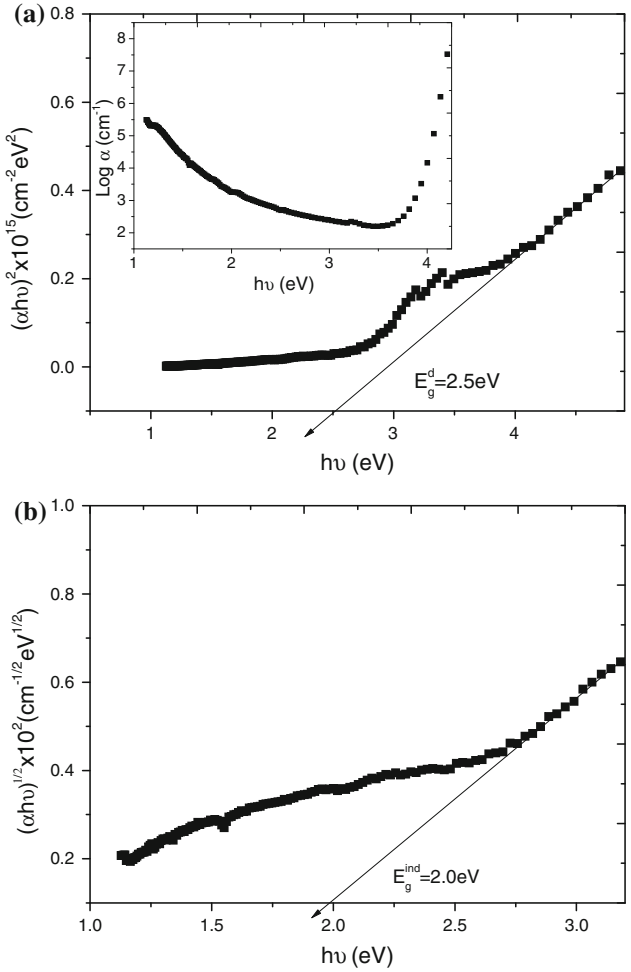

Fig. 8 The plot of **a** $(\alpha h\upsilon)^2$ against photon energy hυ. *Inset* shows the spectral variation of absorption coefficient as a function of the photon energy, **b** $(\alpha h\upsilon)^{1/2}$ against photon energy hυ

The plot reveals continuous decreases in absorption coefficient with corresponding increase in photon energy. The data were analyzed using the following relation for optical absorption in a semiconductor material [33]:

$$\alpha\hbar\omega = k(\hbar\omega - E_g)^{\frac{n}{2}} \tag{6}$$

where k is a constant, E_g is the separation between the valence and conduction bands, and n is a constant which determines the type of the optical transition. Extrapolating the straight line portion of the plots of $(\alpha h\upsilon)^2$ and $(\alpha h\upsilon)^{1/2}$ against hυ to energy axis for zero absorption coefficient gives optical band gap energy. For $n = 1$, the photon energy range 1.0–5.0 eV indicates a direct transition, and for $n = 4$, the photon energy range 1.0–3.25 eV indicates an indirect transition. Figure 8a, b depict the variation of both $(\alpha h\upsilon)^2$ and $(\alpha h\upsilon)^{1/2}$ versus photon energy (hυ). The estimated values of indirect (E_g^{ind}) and direct (E_g^d) band gaps were found to be 2.0 and 2.50 eV respectively, which is in good agreement with the reported gap value (E_g^d) for ZrOS structure obtained by density functional theory calculations [18].

4 Conclusion

In summary, we have obtained with success the *t*-ZrOS powder by sol–gel method. The xerogel isothermally treated at 450 °C for 2 h shows the tetragonal sulfur mediated zirconia, ZrOS which was examined by XRD. The XRD evidently indicated formation of the aforesaid crystalline structure with particle size, of a few nanometers (<16 nm). Optical absorption studies confirmed low absorbance <40 %, indirect and direct optical band gap energy close to 2.0 and 2.50 eV respectively. The high frequency dielectric constant ε_∞ and concentration to effective mass ratio was determined to be 2.22 and $9.72 \times 10^{37}\text{cm}^{-3}$ respectively. The refractive index showed a peak at ~340 nm in the dispersion region. EDX showed the complete removal of chlorine after heat treatment with phase formation of ZrOS powder at different peaks in the energy spectrum. We hope that the work can lead to the acceptance of chemically deposited ZrOS as a prospective component in thin film photovoltaic applications and as dielectric material.

References

1. Peshev P, Stambolova I, Vassilev S, Stefanov P, Blaskov V, Starbova K, Starbov N (2003) Mater Sci Eng B 97:106–110
2. Ro Y-A, Kim S-J, Lee Y-K, Kim CH (2001) Bull Korean Chem Soc 22:1231
3. Chen L, Liu Y, Li Y (2004) J Alloys Compd 381:266–271
4. Quan ZW, Wang LS, Lin J (2005) Mater Res Bull 40:810
5. Jia R, Yang W, Bai Y, Li T (2006) Opt Mater 28:246
6. Maeda N, Wada N, Onoda H, Maegawa A, Kojima K (2003) Thin Solid Films 445:382
7. Assefa Z, Haire RG, Raison PE (2004) Spectrochim Acta A 60:89
8. Kiisk V, Sildos I, Lange S, Reedo V, Tatte T, Kirm M, Aarik J (2005) Appl Surf Sci 247:412
9. De la Rosa E, Diaz-Torres LA, Salas P, Rodrı′guez RA (2005) Opt Mater 27:1320
10. Cabello G, Lillo L, Caro C, Chornik B, Soto MA, delRı′o R, Tejos M (2010) J Phys Chem Solids 71:1367–1372
11. Steele BCH, Drennan J, Slotwinski RK, Bonanos N, Butler EP (1981) Adv Ceram 3:286
12. Badwall SPS (1990) Appl Phys A 50:449
13. Yamaguchi T (1994) Catal Today 20:199
14. Atik M, Aegerter MA (1992) J Non Cryst Solids 813:147–148
15. Celik E, Avci E, Hascicek YS (2000) Phys C 340:193
16. Hauser OZ (1907) Anorg Chem 53:74
17. McCullough JD, Brewer L, Bromley LA (1948) Acta Cryst 1:287
18. Malyi OI, Wu P, Kulish VV, Bai K, Chen Z (2012) Solid State Ion 212:117–122
19. Licheron M, Jouan G, Husson E (1997) J Eur Ceram Soc 17:1453–1457

20. Vallet-Regı′ M, Nicolopoulos S, Roma′n J, Martı′nez JL, Gonza′lez-Calbet JM (1997) J Mater Chem 7:1017
21. Stryckmans O, Segato T, Duvigneaud PH (1955) In: Tranchina BS, Bellosi A (eds) Fourth euroceramics, vol 9. Gruppo Editoriale Faenza Editrice S.p.a, Italy
22. Stelzer NHJ, Schoonman J (1996) J Mater Synth Process 4:429
23. Ruiz H, Vesteghem H, Di Giampaolo AR, Lira J (1997) Surf Coat Technol 89:77
24. Wells AF (1984) Structural inorganic chemistry. Clarendon Press, Oxford, p 487
25. Mikó A, Demirel AL, Somer M (2010) Mater Sci Eng 12:12–19
26. Cullity BD, Stock SR (2001) Elements of X-ray diffraction, 3rd edn. Prentice Hall, Upper Saddle River, p 388
27. Joy K, John Berlin I, Nair PB, Lakshmi JS, Daniel PG, Thomas PV (2011) J Phys Chem Solids 72:673–677
28. Moss TS (1973) Semiconductor opto-electronics. Butterworth, London, p 48
29. Pankove JI (1971) Optical processes in semiconductors. Dove, New York, p 103
30. Sze SM (1981) Physics of semiconductor devices. Wiley, New York
31. Spitzer WG, Fan HV (1957) Phys Rev 166:882
32. Reyna-Garcia G, Garcia-Hipolito M, Guzman-Mendoza J, Aguilar-Frutis M, Falcony C (2004) J Mater Sci Mater Electron 15:439–446
33. Moss TS (1973) Semiconductor opto-electronics. Butterworth, London, p 48